

Error Analysis for Digital Beamforming Synthetic Aperture Radars: A Comparison of Phased Array and Array-Fed Reflector Systems

Sigurd Huber^{ID}, Marwan Younis^{ID}, *Fellow, IEEE*, Gerhard Krieger^{ID}, *Fellow, IEEE*,
and Alberto Moreira^{ID}, *Fellow, IEEE*

Abstract—Modern synthetic aperture radar (SAR) systems for Earth observation from space employ innovative hardware concepts. The key idea is to digitize the output of a multielement antenna almost immediately after the receiver and to dynamically process these data either onboard the radar satellite in real time or on the ground. This article addresses the performance of such digital beamforming (DBF) systems in the presence of phase and magnitude errors in the digital channels. For this, analytic expressions for the sensitivity and range ambiguity performance are derived. These equations are kept general so that they are valid for both planar array antennas and array-fed reflector antennas. It is an important objective of this article to compare these two antenna types to each other. A major conclusion from this analysis is that direct-radiating phased arrays are inherently more susceptible to random phase and magnitude errors compared with array-fed reflector antenna-based systems. This manifests itself in a more rapid degradation of the imaging performance with phased array antennas.

Index Terms—Array-fed reflector, digital beamforming (DBF), error analysis, phased array, synthetic aperture radar (SAR).

I. INTRODUCTION

TRADITIONALLY, synthetic aperture radar (SAR) systems for Earth observation employ phased array antennas [4], [8], [14], [23], [24] that are electronically steerable in order to collect data from a certain region on the ground. This allows imaging swath widths in the stripmap mode in the order of a few tens of kilometers or several hundreds of kilometers in the ScanSAR mode but with reduced azimuth resolution. Modern SAR sensors are required to cover rather a few hundred kilometer wide swaths at an even higher resolution. This gives rise to new SAR system concepts that feature so-called multichannel architectures. This means that these sensors simultaneously acquire data with multiple digital receivers and have the data processed either directly onboard the spacecraft or on the ground. Moreover, antenna types with a long heritage, for instance, in satellite communications are being given consideration in the field of SAR imaging, namely, large deployable reflector antennas,

fed by phased arrays [9], [18], [20]. The motivation for such antenna concepts here is clearly the potential to provide very large apertures, with the goal of improving the sensitivity of the SAR system and the ambiguity performance. Nevertheless, as performance requirements further increase in the future, sophisticated radar architectures in conjunction with powerful radar signal processing techniques will have to fill the gap between these requirements and what is physically feasible.

In reality, however, it is obvious that systematic and random errors impair the performance of a microwave system. For example, during operation, the transmit/receive modules of an SAR sensor will heat up and can cause fluctuations of the magnitude and phase settings, if not compensated properly. Uncalibrated errors such as these will introduce beamforming errors, which could manifest themselves in a degraded sensitivity and ambiguity suppression performance. Other error sources affecting SAR imaging can be residual calibration errors, imprecise antenna pattern knowledge, electromagnetic coupling, attitude, and direction of arrival uncertainties or quantization errors.

On the antenna level, publications dating back as far as to the 1950s have investigated the effects of random and systematic errors, such as surface errors, phase and amplitude quantization errors or element position errors on the antenna pattern shape, beam pointing, and sidelobe levels [3], [11], [12], [19], [22], [25], [28]. These articles address and compare array-fed reflector antennas and direct-radiating large aperture antennas consisting of many elements. With the commissioning of Earth observation satellites employing large phased array antennas, error investigations have been conducted for instance for the Radarsat-2 mission [8] or the TerraSAR-X/TanDEM-X missions [2], [5]. Recently, new SAR system concepts with multiple digital channels and massive onboard processing again raised the question on their calibration requirements and sensitivity against various error sources [1], [7], [15].

The focus of this work lies on an SAR performance comparison of phased array and array-fed reflector antenna-based systems, featuring multichannel hardware architectures. In contrast to [7], we consider beamforming in elevation. Based on an SAR signal model in Section II, an error model is introduced in Section II-A. The SAR antenna

Manuscript received June 26, 2020; revised August 21, 2020; accepted September 29, 2020. Date of publication October 20, 2020; date of current version July 22, 2021. (Corresponding author: Sigurd Huber.)

The authors are with Microwaves and Radar Institute, German Aerospace Center (DLR), 82234 Oberpfaffenhofen, Germany (e-mail: sigurd.huber@dlr.de).

Digital Object Identifier 10.1109/TGRS.2020.3029680

concepts and beamforming techniques are introduced in Sections II-B and II-C, respectively. The performance for a spaceborne SAR scenario is presented in Section III, which is complemented by considerations on antenna level in Section IV. A discussion in Section V concludes this article.

II. SAR SIGNAL MODEL

SAR imaging employing digital beamforming (DBF) can be described by the following time-domain point target signal model:

$$\begin{aligned} u(t) &= \sum_i w_i(t) e_i \left[\sum_k s(t, \vartheta_k(t)) a_i(\vartheta_k(t)) + v_i(t) \right] \\ &= \sum_i w_i e_i \left[\sum_k s_k a_{ik} + v_i \right]. \end{aligned} \quad (1)$$

Since we are focusing on beamforming in the range or elevation direction, denoted by the continuous angular variable ϑ_k , the azimuthal variable shall be omitted for a clearer representation. The summation index k refers to range ambiguities, superimposing the signal of interest ($k = 0$). In this context, w_i denotes time-variant beamforming coefficients, i counting the receive channels, which are adjusted with a certain update rate in accordance with the SAR pulse propagating across the swath. Here, very short pulses have been assumed such that the beamforming operation can be represented by simple multiplication with a complex coefficient, instead of a filtering operation. The variable s incorporates the transmit waveform, the propagation paths from the transmitter to ground and back to the receiver, and the backscatter function and other constant terms. The functions a_i describe the two-way antenna patterns, including the transmit and receive patterns, while v_i represents additive white Gaussian receiver noise. In this model, errors have been introduced by the multiplicative terms e_i . In the context of this article, these errors shall refer to the receiver only, which is a reasonable assumption for SAR systems with a single transmit channel. This approach might have to be modified when looking at multitransmitter architectures.

Based on the signal model (1), typical SAR performance metrics, namely, the noise equivalent sigma zero (NESZ) and the range ambiguity-to-signal ratio (RASR), shall be derived. For this, we have to take the power of the beamformer output signal $u(t)$

$$\begin{aligned} \mathcal{E}\{|u(t)|^2\} &= P_{s_k} + P_v \\ &= \mathcal{E}\left\{\left|\sum_i w_i e_i \sum_k s_k a_{ik}\right|^2\right\} \\ &\quad + \mathcal{E}\left\{\left|\sum_i w_i e_i v_i\right|^2\right\} \end{aligned} \quad (2)$$

where the thermal noise v_i has been assumed uncorrelated with signal and range ambiguities s_k . Note that, here, a very contracted notation of the expectation operator \mathcal{E} has been used. It shall refer to the errors e_i , signal and range ambiguities s_k , and thermal receiver noise v_i . Evaluating (2) further,

one arrives at power expressions for the signal and range ambiguities P_{s_k} and the thermal noise P_v

$$\begin{aligned} P_{s_k} &= \sum_i \sum_j w_i w_j^* \mathcal{E}\{e_i e_j^*\} \sum_k \sum_l \mathcal{E}\{s_k s_l^*\} a_{ik} a_{jl}^* \\ &= \sum_i \sum_j w_i w_j^* \mathcal{E}\{e_i e_j^*\} \sum_k \sigma_{s_k}^2 a_{ik} a_{jk}^* \end{aligned} \quad (3)$$

$$\begin{aligned} P_v &= \sum_i \sum_j w_i w_j^* \mathcal{E}\{e_i e_j^*\} \mathcal{E}\{v_i v_j^*\} \\ &= \sum_i |w_i|^2 \mathcal{E}\{|e_i|^2\} \sigma_{v_i}^2. \end{aligned} \quad (4)$$

In (3), mutually uncorrelated signal and range ambiguities have been postulated. This assumption shall also apply to the thermal noise of the receive channels in (4). We have taken zero mean distributions for the thermal noise and the signal and range ambiguities, with variances $\sigma_{v_i}^2$ and $\sigma_{s_k}^2$, respectively. Note that, in the frame of SAR imaging, $\sigma_{s_k}^2$ is usually related to the backscatter coefficient σ^0 .

A. Error Model

Except being multiplicative, the error in (1) is kept quite general. An accepted model in the literature is the following [11], [25]:

$$e_i = (1 + \zeta_i) e^{j\tilde{\zeta}_i}. \quad (5)$$

In the context of SAR imaging, it would describe magnitude and phase errors, ζ_i and $\tilde{\zeta}_i$, respectively. Those are typical errors encountered when setting, for instance, gain and phase of SAR system's transmit/receive modules. In a simple approach, one might assume zero mean magnitude errors¹ with standard deviation σ_{ζ_i} and phase errors uniformly distributed in an interval $[-\Delta\zeta_i/2, \Delta\zeta_i/2]$ with the corresponding probability density function

$$p_{\zeta_i}(\zeta_i) = \frac{1}{\Delta\zeta_i} \text{rect}(\zeta_i; \Delta\zeta_i). \quad (6)$$

Note that, for a uniform distribution, the standard deviation σ_{ζ_i} is related to the interval $\Delta\zeta_i$ via

$$\sigma_{\zeta_i} = \frac{\Delta\zeta_i}{\sqrt{12}}. \quad (7)$$

Now, the expectations $\mathcal{E}\{e_i e_j^*\}$ in (3) and (4) can be calculated according to² (see the Appendix)

$$\mathcal{E}\{e_i e_j^*\} = \delta_{ij} (1 + \sigma_{\zeta_i}^2) + (1 - \delta_{ij}) \text{sinc} \frac{\Delta\zeta_i}{2} \text{sinc} \frac{\Delta\zeta_j}{2} \quad (8)$$

where δ_{ij} denotes the Kronecker delta. Here, again, we have taken the errors ζ_i and $\tilde{\zeta}_i$ to be mutually uncorrelated. This presumption should be regarded rather pessimistic with regard to the performance degradation since, in a real system, there could be correlations for instance due to a uniform heating

¹This is an approximation since magnitude errors are usually asymmetrically distributed, and therefore, the expectations $\mathcal{E}\{\zeta_i\}$ would not vanish. However, for small errors, this assumption is reasonable.

²An even simpler model might assume an error phasor with both components, real-part and imaginary part, Gaussian distributed $e_i = 1 + \zeta_i + j\tilde{\zeta}_i$. In this case, the expectation $\mathcal{E}\{e_i e_j^*\}$ would result in $1 + \delta_{ij} \sigma_{\zeta_i}^2 + \delta_{ij} \sigma_{\tilde{\zeta}_i}^2$.

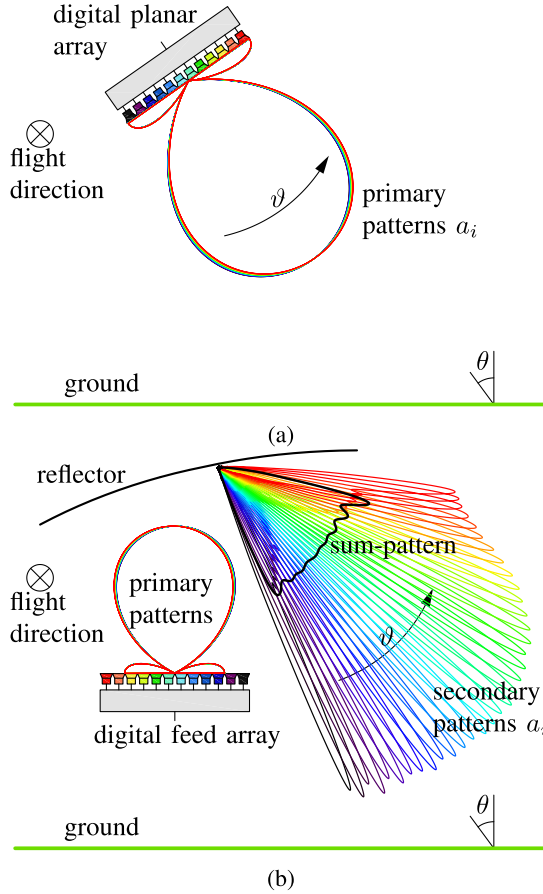


Fig. 1. Side-looking SAR system with a digital multichannel receiver. (a) Classical phased array SAR illuminates the swath on the ground with its primary patterns, each associated with a digital channel. (b) In contrast, an array-fed reflector SAR uses its secondary patterns to illuminate the swath on the ground. The difference between both concepts lies in the shape of the far-field patterns a_i .

of the transmit/receive modules. This means that, in reality, the performance degradation might not be as severe. For the remainder of this article, we shall introduce a further simplification such that the magnitude and phase error standard deviations are taken constant across the receive channels, with $\sigma_{\xi_i} = \sigma_{\xi}$ and $\sigma_{\zeta_i} = \sigma_{\zeta}$.

B. SAR Antenna Concepts

So far, we have not made any specifications regarding the SAR antenna. In (1), the functions a_i represent, quite generally, the far-field patterns of a multireceiver antenna. Here, two antenna concepts shall be contrasted with each other: the first being a phased array-based SAR system and the second an array-fed reflector SAR system. Fig. 1(a) sketches a side-looking SAR with a planar array antenna. The sensor flies into the paper plane (azimuth direction), while scanning is performed in the paper plane (angle ϑ). Each primary pattern a_i , indicated by the rainbow color code, illuminates the same region on the ground. In contrast, Fig. 1(b) shows a reflector-based SAR system. Here, the primary patterns of the feed array are directed toward a reflector with a circular aperture, which transforms these primary patterns into so-called

TABLE I
ANTENNA PARAMETERS FOR A PLANAR ARRAY ANTENNA AND AN ARRAY-FED REFLECTOR. THE ANTENNAS HAVE BEEN SIMULATED AT 1.2575 GHz ($\lambda = 0.2384$ m)

antenna	reflector	planar array
diameter / size	$D_{\text{ref}} = 15$ m	$D_{\text{pla}} = 11$ m
focal length	13.5 m	-
offset	9 m	-
elements	35	35
spacing	0.6591λ	1.3183λ

secondary patterns. The secondary patterns illuminate essentially nonoverlapping regions on the ground. Summing up all secondary patterns yields a broad pattern, which shall serve as an illuminating source of the swath on the ground. Insofar direct-radiating arrays fundamentally differ from array-fed reflectors by their pattern characteristics. This should manifest in different behavior under error conditions.

For the purpose of comparison, a planar array antenna and an array-fed reflector antenna have been simulated, with the most important parameters given in Table I. The choice of a frequency of 1.2575 GHz was motivated by investigations of SAR missions at the L-band but has no deeper meaning beyond this. More details regarding the array-fed reflector can be found, for example, in [10]. In order to have a fair comparison, both antennas shall possess the same number of elements (digital channels) and the same half-power beamwidth $\vartheta_{3 \text{ dB}}$ at boresight, which may be approximated according to

$$\vartheta_{3 \text{ dB}} \approx 1.22 \frac{\lambda}{D_{\text{ref}}} \approx 0.89 \frac{\lambda}{D_{\text{pla}}} = 1.1^\circ. \quad (9)$$

This results in a relatively large antenna elevation dimension D_{pla} of 11 m. For the sake of performance comparison, the planar array size in azimuth is taken to be 11 m resulting in a square aperture. Note that, current SAR satellites, such as the RADARSAT-2 satellite [21], usually employ antenna sizes of more than 10 m in only one dimension while having a relatively small size in the other dimensions. However, since this example here is only meant for meaningful performance comparison, a similar analysis for instance at the X-band would lead to feasible antenna sizes according to the state of the art.

The larger prefactor for the array-fed reflector is a consequence of the circular aperture and also the illumination-taper by the primary patterns [17], as indicated in Fig. 1(b).

C. Beamforming

In order to derive beamforming coefficients w_i , we switch to the more convenient vector-matrix notation and reformulate (1) according to

$$u = \mathbf{w}^T \left(\sum_k s(\vartheta_k) \mathbf{a}(\vartheta_k) + \mathbf{v} \right) \quad (10)$$

where we have omitted the time variable t for a clearer representation. Important to mention here is that the beamforming coefficients will be computed from an error-free signal model. This approach is reasonable unless these errors are known

a priori and characterized well. In this case, one would deal with the complete equation

$$u = \mathbf{w}^T \mathbf{E} \left(\sum_k s(\vartheta_k) \mathbf{a}(\vartheta_k) + \mathbf{v} \right) \quad (11)$$

$$= \mathbf{w}^T \left(\sum_k s(\vartheta_k) \mathbf{a}_e(\vartheta_k) + \mathbf{v}_e \right) \quad (12)$$

including the error terms on the main diagonal of the matrix \mathbf{E} . Mathematically, this equation is equivalent to (10), which allows formulating the following optimization problem [16]:

$$\min \mathbf{w}^T \mathbf{R}_v \mathbf{w}^* \quad (13)$$

$$\text{s.t. } \mathbf{w}^T \mathbf{a}(\vartheta_0) = 1 \quad (14)$$

$$|\mathbf{w}^T \mathbf{a}(\vartheta_{SL})|^2 \leq \eta_{SL}, \quad \vartheta_k \in \vartheta_{SL}. \quad (15)$$

Equation (13) represents the noise power [see (4)] to be minimized, with $\mathbf{R}_v = \mathcal{E}\{\mathbf{v}\mathbf{v}^H\}$ being the noise channel covariance matrix. Equation (14) is a mainbeam constraint, causing a beampointing at ϑ_0 , and (15), which, in fact, resembles a set of equations, introduces sidelobe constraints. In the following, we concentrate on two beamforming techniques, where the first one is known as minimum variance distortionless response (MVDR) beamforming. This beamformer takes only the mainbeam constraint (14) into account and has the analytic solution

$$\mathbf{w}^* = \frac{\mathbf{R}_v^{-1} \mathbf{a}(\vartheta_0)}{\mathbf{a}^H(\vartheta_0) \mathbf{R}_v^{-1} \mathbf{a}(\vartheta_0)}. \quad (16)$$

As the second beamforming concept, we use the complete set of constraints and try to minimize entire sidelobe regions where the most dominant range ambiguities can be expected. In this article, this technique shall be referred to as sidelobe-constrained MVDR beamforming.

III. COMPARISON—SAR PERFORMANCE

Having established the theoretical foundation, we can now define the performance parameters, based on error model (5), to be investigated for the planar direct-radiating array and the array-fed reflector, using MVDR beamforming and its sidelobe-constrained version

$$\text{NESZ} := \frac{P_b}{P_{s_0}/\sigma^0(\theta_0)} \quad (17)$$

$$\text{RASR} := \frac{P_{s_{k,k \neq 0}}}{P_{s_0}}. \quad (18)$$

For the computation of the signal, ambiguity, and noise power, using (3) and (4), the terms $\sigma_{s_k}^2$ and σ_v^2 may be found in agreement with the standard SAR literature [6] according to

$$\sigma_{s_k}^2 = \frac{P_{Tx} \lambda^3 c \cdot dc \cdot \sigma^0(\theta_k)}{4^4 \pi^3 v_{sat} L_{sys} r_k^3 \sin \theta_k} \quad (19)$$

$$\sigma_v^2 = k_B T_0 B F_{sys} \quad (20)$$

$$r_k = r_0 + k/\text{PRF} \quad (21)$$

assuming equal noise power in each receive channel (see Table II for an explanation of the individual parameters). It should be mentioned that, in the subsequent performance evaluations, the NESZ and the RASR have been evaluated at

TABLE II
SIMULATION PARAMETERS ASSUMING A TANDEM-L SCENARIO

parameter	symbol	value
orbit height		740 km
satellite velocity	v_{sat}	7484 m/s
antenna boresight angle		32.2°
minimum incident angle		26.3°
backscatter model	σ^0	short vegetation [26]
swath width		350 km
k th distance	r_k	variable
k th incident angle	θ_k	variable
peak Tx power (refl. / pla.)	P_{Tx}	4862 W / 4950 W
system losses	L_{sys}	3.6 dB
system noise figure	F_{sys}	3.5 dB
pulse duty cycle (refl. / pla.)	dc	4 % / 5 %
pulse repetition frequency	PRF	2.6 kHz
bandwidth	B	84 MHz
reference temperature	T_0	290 K
speed of light	c	2.998×10^8 m/s
Boltzmann's constant	k_B	$1.38 \times 10^{-23} \frac{\text{m}^2 \text{kg}}{\text{s}^2 \text{K}}$

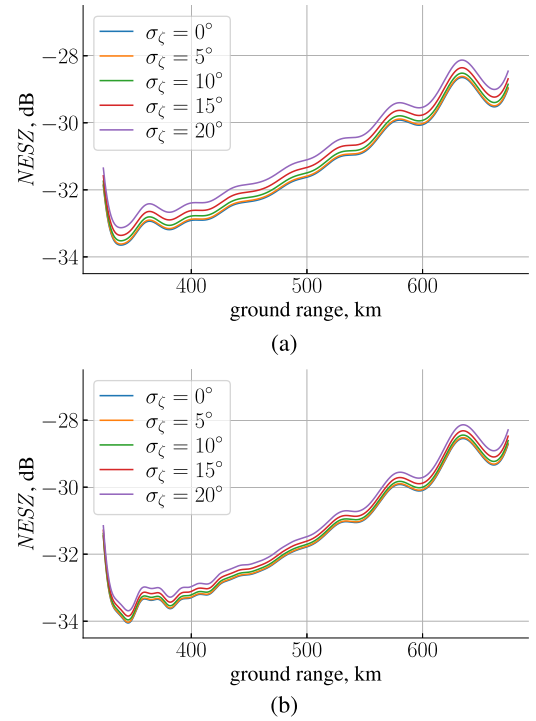


Fig. 2. Expected NESZ with MVDR beamforming versus ground range for different phase error standard deviation levels σ_ζ . In both cases, (a) and (b), and in all subsequent simulations, as transmit pattern, the sum-pattern as presented in Fig. 1(b) has been used. (a) Planar array antenna. (b) Array-fed reflector antenna.

zero Doppler frequency, which is a good approximation to the case when an azimuth integration of the Doppler spectra is taken into account.

For the purpose of performance comparison, the Tandem-L mission proposal [10], [13], [18] shall serve as a simulation scenario, with the most important parameters relevant for (19)–(21) listed in Table II. Fig. 2 shows the expectation value of the NESZ for the planar array SAR in plot (a) and for the array-fed reflector SAR in plot (b). Here, MVDR beamforming

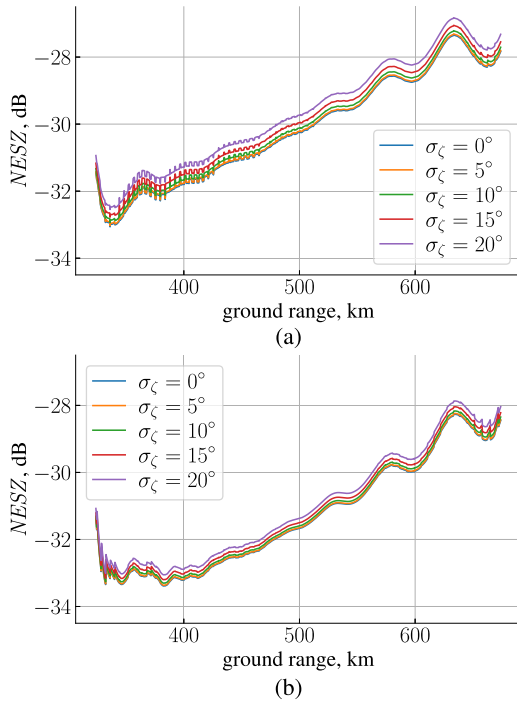


Fig. 3. Expected NESZ with sidelobe-constrained MVDR beamforming versus ground range for different phase error standard deviation levels σ_ζ . (a) Planar array antenna. (b) Array-fed reflector antenna.

according to (16) has been used. The curves refer to different levels of phase error standard deviations σ_ζ , where $\sigma_\zeta = 0^\circ$ represents the error-free or nominal case. While an error level of 5° is a realistic assumption for present-day SAR satellites, the values larger than this may be considered unlikely to occur in real systems. Here, their purpose is to give the reader an impression of their effect on the beamforming performance. The same can be said about the choice of the magnitude error levels presented in Section IV.

In terms of performance, there is not much difference between the planar array and the array-fed reflector, except that the NESZ degrades slightly faster with increasing phase errors for the planar system. This picture does not change much with sidelobe-constrained MVDR beamforming, as can be seen in Fig. 3. However, a general loss in NESZ can be observed. This is a consequence of the sidelobe constraints, which usually means sacrificing gain in the mainbeam direction. In the case of the planar array antenna, this NESZ loss is almost 2 dB and, therefore, significantly more compared with the reflector antenna. This fact may be attributed to a lack of spatial orthogonality of the element patterns of the planar array. The small discontinuities in the near and far range are the artifacts of the beamforming weight optimization, which is reinitialized for each ground range sample.

The range ambiguity performance with MVDR beamforming is presented in Fig. 4. Here, a qualitative and quantitative difference between the planar and the array-fed reflector SAR system becomes apparent. It seems that reflector SAR systems become more susceptible to phase errors when the range ambiguities occur in the natural minima in the sidelobe regions. These minima get smeared, and noticeable degradation of

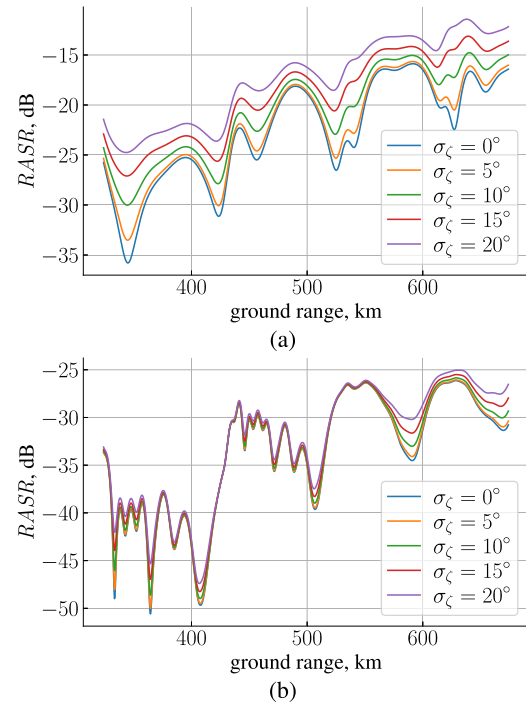


Fig. 4. Expected RASR with MVDR beamforming versus ground range for different phase error standard deviation levels σ_ζ . (a) Planar array antenna. (b) Array-fed reflector antenna.

the RASR can be observed [see Fig. 4(b)]. This changes drastically with a planar array antenna as can be concluded from Fig. 4(a). Here, with increasing phase error standard deviation, an almost homogeneous degradation of the RASR across the swath can be noticed. This behavior is even more pronounced with sidelobe-constrained MVDR beamforming, as depicted in Fig. 5, where a sidelobe constraint η_{SL} of -50 dB compared with the mainlobe maximum has been set. In the nominal case ($\sigma_\zeta = 0^\circ$), both SAR systems are capable of suppressing range ambiguities below a level of -40 dB. However, in contrast to the reflector SAR system, the ambiguity rejection performance changes dramatically for the planar system. Phase errors with a standard deviation in the order of 5° are sufficient to worsen the RASR by roughly 20 dB, as it can be observed in Fig. 5(a). In comparison, the array-fed reflector SAR shows a significantly lower susceptibility to random phase errors.

For a better understanding of the beamforming process, we can study the effects of phase errors on the gain pattern examples shown in Fig. 6 versus scan angle ϑ . In this context, the vertical red dashed lines mark the directions of the range ambiguities, while the green dashed line denotes the signal direction, corresponding to the rightmost ground range sample in the above NESZ and RASR plots. Here, the gain patterns for the nominal case and a phase error standard deviation of 5° are presented. As it can be noticed in Fig. 6(a), the planar array antenna loses, almost completely, the suppression of the sidelobes, whereas the array-fed reflector maintains its pattern shape in the sidelobe region much better [see Fig. 6(b)].

Fig. 7 shows the complex beamforming coefficients corresponding to the pattern plots without phase error presented

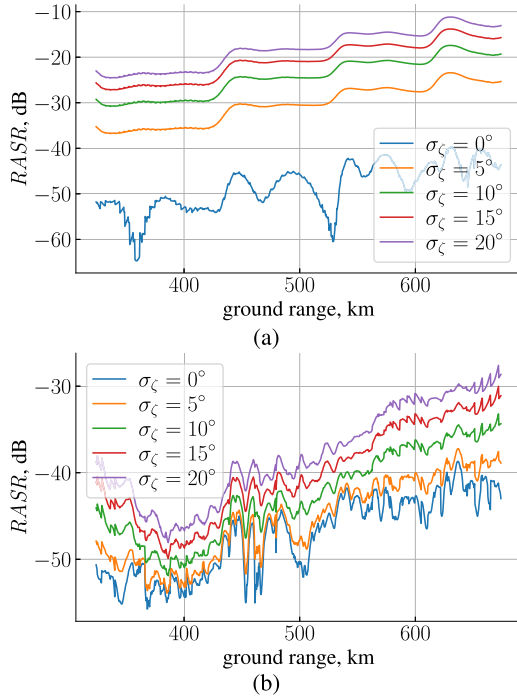


Fig. 5. Expected RASR with sidelobe-constrained MVDR beamforming versus ground range for different phase error standard deviation levels σ_ζ . (a) Planar array antenna. (b) Array-fed reflector antenna.

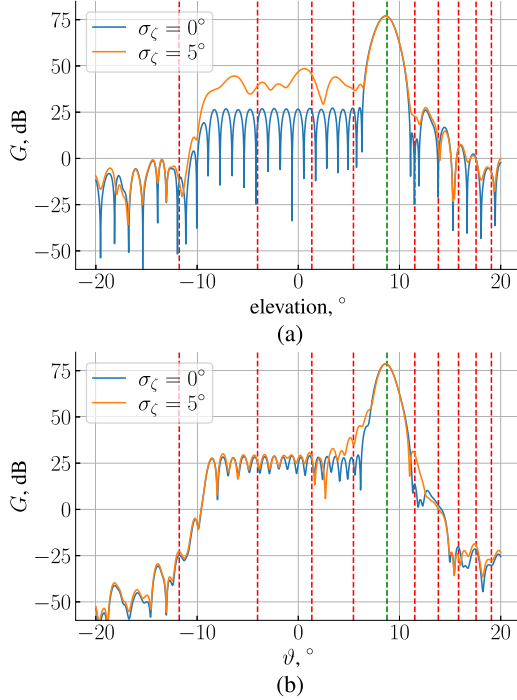


Fig. 6. Example of two-way antenna gain patterns versus elevation angle using sidelobe-constrained MVDR beamforming. (a) Planar array antenna. (b) Array-fed reflector antenna.

in Fig. 6. Here, it becomes evident that, in the reflector case, only a few feed elements carry power, while, in the planar case, almost all elements contribute.

IV. COMPARISON—ANTENNA PERFORMANCE

It is worthwhile to make a comparison between the two systems on the antenna level. Such a scene and imaging

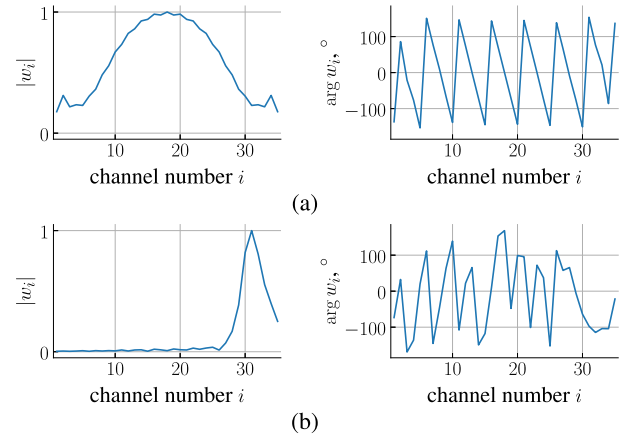


Fig. 7. Sidelobe-constrained MVDR beamforming coefficients (left: magnitude and right: phase) corresponding to the error-free pattern examples shown in Fig. 6. (a) Planar array antenna. (b) Array-fed reflector antenna.

geometry-independent approach should give a deeper insight into the beamforming performance under error conditions. For this, we define the signal-to-noise ratio (SNR) and the signal-to-interference ratio (SIR) according to

$$\text{SNR} := \frac{P_{s_0}}{P_v} \quad (22)$$

$$\text{SIR} := \frac{P_{s_0}}{P_{s_{k,k \neq 0}}} \quad (23)$$

with

$$\sigma_{s_k}^2 = \sigma_{v_i}^2 = 1. \quad (24)$$

Note that, in this context, the SNR could also be interpreted as the antenna gain on receive. If we ask the question how much sensitivity and interference suppression are lost in the presence of errors, we can define the following loss figures:

$$L_{\text{SNR}} := \frac{\text{SNR}(e=1)}{\text{SNR}} \quad (25)$$

$$L_{\text{SIR}} := \frac{\text{SIR}(e=1)}{\text{SIR}}. \quad (26)$$

Here, the error-free values ($e=1$) of the SNR and the SIR are related to the erroneous ones in the denominator. It is clear that these loss figures depend not only on the phase and magnitude errors but also on the direction of the mainbeam and the number and directions of the ambiguities to be suppressed. The SNR and SIR loss shall be evaluated exactly at the same location as the patterns given in Fig. 6, namely, at the far end of the swath.

Fig. 8 shows the SNR loss for both antenna types versus phase error standard deviation σ_ζ . Note that, according to formula (7), a phase error standard deviation of 103.9° corresponds to phase errors uniformly distributed between $\pm 180^\circ$. The parameter for the curves is now the magnitude error standard deviation σ_ξ [see (5)]. The first observation is that the loss curves converge to a singular value for large phase errors. However, for the planar antenna, this maximum loss is much bigger compared with the array-fed reflector. This can be explained by analytically evaluating the loss figure (25).

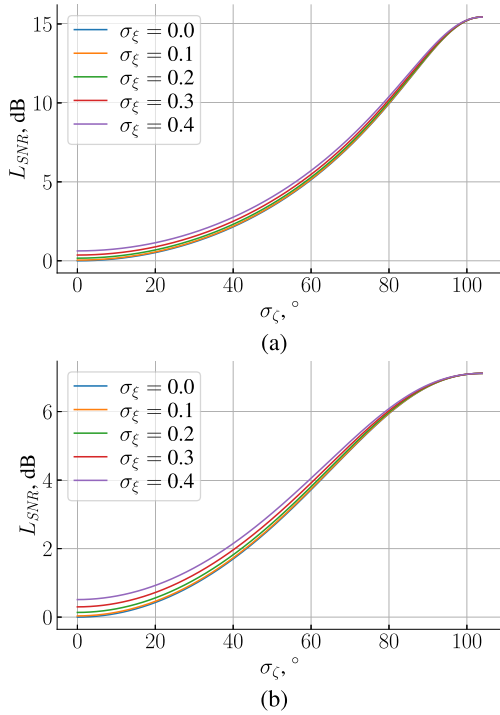


Fig. 8. Expected SNR loss with MVDR beamforming as a function of the phase error (parameterized for different magnitude errors). (a) Planar array antenna. (b) Array-fed reflector antenna.

In antenna boresight direction ($\vartheta = 0^\circ$) and with MVDR beamforming, one can use the simplification $w_i = a_i = 1$, and by substituting (3)–(5) into (25), one arrives at

$$L_{SNR} = \frac{N}{1 + \frac{\text{sinc}^2(\Delta\zeta/2)}{1 + \sigma_\zeta^2} (N - 1)} \quad (27)$$

where N is the number of array elements. Now, it becomes clear that, for phase error intervals $\Delta\zeta$ of 360° and/or infinitely large magnitude error standard deviations σ_ξ , the loss in SNR or antenna gain becomes N , which is 35 or 15.4 dB in our example.³ Of course, the number of array elements for a given antenna size D_{pla} is bounded by a minimum element spacing Δ_{min} , and $N < D_{\text{pla}}/\Delta_{\text{min}}$, such that the loss cannot become infinite. In contrast, the array-fed reflector is much less prone to such severe SNR losses. This is due to the fact that only a few feed elements, in the order of two to five feed elements, contribute to a given signal direction. In the far range, the beams are more defocused compared with the swath center, which means that, in the far range, the loss is larger. At the swath center, this worst case loss can be as low as 3 dB.

Regarding the interference suppression loss L_{SIR} , which is presented in Fig. 9, there is also a significant difference between planar array antennas and array-fed reflectors. Again, one observes that all the curves converge to a single worst case loss value for a phase error standard deviation of 103.9° . In the case of the planar array system, as presented in Fig. 9(a), we may be able to give an estimate of this worst case loss.

³The example in Fig. 8(a) is not a boresight situation, but the scan-loss is negligible, so that the maximal loss in this example is almost exactly 15.4 dB.

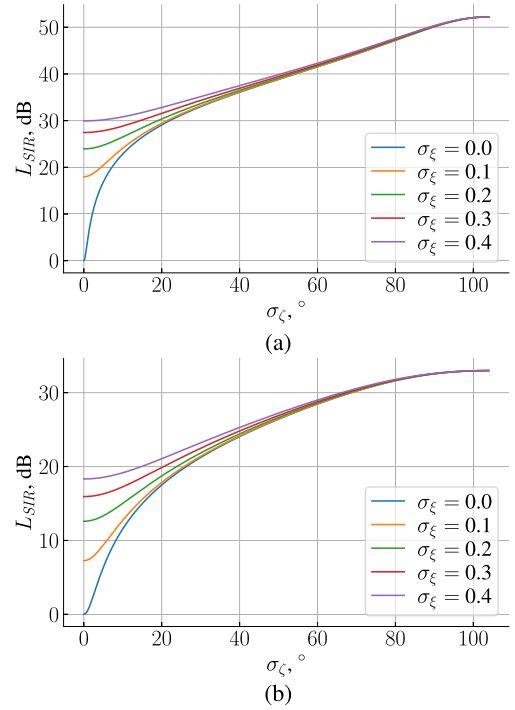


Fig. 9. Expected SIR loss with sidelobe-constrained MVDR beamforming as a function of the phase error (parameterized for different magnitude errors). (a) Planar array antenna. (b) Array-fed reflector antenna.

Inserting (3), (5), and (24) into (23) gives us for the error-free and erroneous SIR

$$\begin{aligned} \text{SIR}(\mathbf{e} = \mathbf{1}) &= \frac{\sum_i \sum_j w_i w_j^* a_i a_j^*}{\sum_i \sum_j w_i w_j^* \sum_k a_{ik} a_{jk}^*} \\ &\approx \frac{1}{K \eta_{\text{SL}}} \end{aligned} \quad (28)$$

$$\begin{aligned} \text{SIR}(\sigma_\xi = 0, \sigma_\zeta = 103.9^\circ) &= \frac{\sum_i |w_i|^2 |a_i|^2}{\sum_i |w_i|^2 \sum_k |a_{ik}|^2} \\ &\approx \frac{1}{K} \end{aligned} \quad (29) \quad (30)$$

where K is the number of range ambiguities [number of angles ϑ_k in constraint (15)]. Combining these results yields for the interference suppression loss roughly

$$L_{\text{SIR}} \approx \frac{1}{\eta_{\text{SL}}} \quad (31)$$

which, for our example in Fig. 9(a), would be 50 dB. For a reflector SAR system [see Fig. 9(b)], it is, of course, much harder to give such a quantitative estimate since, due to a lack of an analytic antenna pattern model a_i , especially expression (29) is hard to evaluate. However, it is clear that, due to the inherently low sidelobes of reflector antennas, the terms $|a_{ik}|^2$ in (29) contribute much less in comparison to a planar array. This explains why, under extreme error conditions, array-fed reflector antennas still are able to suppress range ambiguities to a certain degree.

V. CONCLUSION AND DISCUSSION

This article presents a sensitivity analysis of SAR systems with DBF against random magnitude and phase errors.

We have derived formulas that can be used to estimate the sensitivity and range ambiguity performance of multielevation-channel SAR systems under error conditions. Here, the focus lies on SAR modes with constant pulse repetition frequency PRF. Moreover, the performance has been demonstrated for single- and dual-polarization modes. However, an extension to quad-polarization modes and modes with nonconstant PRF [27] should be straightforward.

Two types of SAR antennas have been opposed to each other: a conventional planar phased array antenna and an array-fed reflector antenna. It turned out that direct-radiating arrays are inherently more sensitive to those kinds of errors. The reason for this lies in the functional principle of these antennas. Since each array element “sees” the same angular far-field domain, direct-radiating arrays require all elements to form, for instance, a narrow high gain beam. The shape of the beam is controlled by the phases and magnitudes of the beamforming weights. In contrast, the functional principle of a reflector antenna is fundamentally different. To form a narrow high gain beam in principle, a single feed element is sufficient if placed at the focal point. This means that the beamforming problem is transformed to a mechanical shaping problem in the reflector case. Insofar, one may conclude that, as long as a reflector is stable against thermal or mechanical deformation, it will always be more robust against random phase and magnitude errors in the transmit/receive modules. Stated differently, direct-radiating arrays are comparatively more prone to this kind of error since beamforming with this type of antenna includes always the whole set of array elements.

Finally, one should remark that once idealizing assumptions, such as on the thermoelastic stability of the reflector antenna aperture or on other geometrical and material tolerances and uncertainties, are dropped, the picture might change and the performance of array-fed reflector antennas may become less superior or even worse compared with planar direct-radiating antenna arrays, depending on the number of geometrical errors considered.

APPENDIX

The expectations $\mathcal{E}\{e_i e_j^*\}$ substituting error model (5) read

$$\mathcal{E}\{e_i e_j^*\} = \mathcal{E}_{\xi_i, \xi_j, \zeta_i, \zeta_j} \left\{ (1 + \xi_i + \xi_j + \xi_i \xi_j) e^{j(\zeta_i - \zeta_j)} \right\}. \quad (32)$$

Here, we have explicitly expressed that the expectations are taken with respect to the independent variables ξ_i , ξ_j , ζ_i , and ζ_j . Now, we can discriminate two cases. For $i = j$, the complex exponential vanishes, and the expectations are

$$\mathcal{E}\{1 + 2\xi_i + \xi_i^2\} = 1 + \sigma_{\xi_i}^2. \quad (33)$$

Note that the term $\mathcal{E}\{2\xi_i\}$ vanishes according to our assumption. In the case when $i \neq j$, the expectations yield

$$\mathcal{E}_{\xi_i, \xi_j} \{e^{j(\zeta_i - \zeta_j)}\} = \text{sinc} \frac{\Delta \zeta_i}{2} \text{sinc} \frac{\Delta \zeta_j}{2}. \quad (34)$$

The results [see (33) and (34)] can then be combined to the single equation (8) using the Kronecker delta.

REFERENCES

- [1] F. Q. de Almeida, S. Huber, M. Jäger, A. Loinger, T. Rommel, M. Villano, and M. Younis, “Calibration and data reduction for digital beam forming instruments,” Eur. Space Agency (ESA/ESTEC), Noordwijk, The Netherlands, Tech. Rep. ESA/ESTEC Contract 4000117363/16/NL/FE, Dec. 2018.
- [2] M. Bachmann, M. Schwerdt, B. Braeutigam, and B. Doering, “Final results of the TerraSAR-X in-orbit antenna model verification,” in *Proc. 7th Eur. Conf. Synth. Aperture Radar (EUSAR)*, Jun. 2008, pp. 1–4.
- [3] R. Bracewell, “Tolerance theory of large antennas,” *IRE Trans. Antennas Propag.*, vol. 9, no. 1, pp. 49–58, Jan. 1961.
- [4] B. Braeutigam, J. H. Gonzalez, M. Schwerdt, and M. Bachmann, “TerraSAR-X instrument calibration results and extension for TanDEM-X,” *IEEE Trans. Geosci. Remote Sens.*, vol. 48, no. 2, pp. 702–715, Feb. 2010.
- [5] B. Braeutigam, J. H. Gonzalez, M. Schwerdt, and M. Bachmann, “Radar instrument calibration of TerraSAR-X,” in *Proc. 7th Eur. Conf. Synth. Aperture Radar (EUSAR)*, Jun. 2008, pp. 1–4.
- [6] J. C. Curlander and R. N. McDonough, *Synthetic Aperture Radar Systems and Signal Processing*. Hoboken, NJ, USA: Wiley, 1991.
- [7] F. Q. de Almeida, M. Younis, G. Krieger, and A. Moreira, “An analytical error model for spaceborne SAR multichannel azimuth reconstruction,” *IEEE Geosci. Remote Sens. Lett.*, vol. 15, no. 6, pp. 853–857, Jun. 2018.
- [8] P. A. Fox and C. Grenier, “The RADARSAT-2 synthetic aperture radar antenna phased array error analysis and performance,” in *Proc. IEEE Int. Symp. Phased Array Syst. Technol.*, Oct. 2003, pp. 25–247.
- [9] F. Helière, A. Carbone, J. G. N. Fonseca, N. Ayllon, A. Barnes, and M. Fehring, “Biomass P-band SAR,” in *Proc. 11th Eur. Conf. Synth. Aperture Radar (EUSAR)*, Jun. 2016, pp. 1–4.
- [10] S. Huber, F. Q. de Almeida, M. Villano, M. Younis, G. Krieger, and A. Moreira, “Tandem-L: A technical perspective on future spaceborne SAR sensors for Earth observation,” *IEEE Trans. Geosci. Remote Sens.*, vol. 56, no. 8, pp. 4792–4807, Aug. 2018.
- [11] E. A. Jaska, L. E. Corey, and S. Y. Park, “Effects of random amplitude and phase errors on monopulse null depth in phased-array antennas,” in *Proc. Int. Symp. Antennas Propag. Soc., Merging Technol.*, vol. 2, May 1990, pp. 836–839.
- [12] W. P. M. N. Keizer, “Low sidelobe phased array pattern synthesis with compensation for errors due to quantized tapering,” *IEEE Trans. Antennas Propag.*, vol. 59, no. 12, pp. 4520–4524, Dec. 2011.
- [13] G. Krieger *et al.*, “Tandem-L: A mission for monitoring Earth system dynamics with high resolution SAR interferometry,” in *Proc. 8th Eur. Conf. Synth. Aperture Radar (EUSAR)*, Jun. 2010, pp. 506–509.
- [14] G. Krieger *et al.*, “TanDEM-X: A satellite formation for high-resolution SAR interferometry,” *IEEE Trans. Geosci. Remote Sens.*, vol. 45, no. 11, pp. 3317–3341, Nov. 2007.
- [15] P. Laskowski, F. Bordon, and M. Younis, “Error analysis and calibration techniques for multichannel SAR instruments,” in *Proc. IEEE Int. Geosci. Remote Sens. Symp. (IGARSS)*, Jul. 2013, pp. 4503–4506.
- [16] J. Liu, A. B. Gershman, Z.-Q. Luo, and K. Max Wong, “Adaptive beamforming with sidelobe control: A second-order cone programming approach,” *IEEE Signal Process. Lett.*, vol. 10, no. 11, pp. 331–334, Nov. 2003.
- [17] T. A. Milligan, *Modern Antenna Design*, 2nd ed. Hoboken, NJ, USA: Wiley, 2005.
- [18] A. Moreira *et al.*, “Tandem-L: A highly innovative bistatic SAR mission for global observation of dynamic processes on the Earth’s surface,” *IEEE Geosci. Remote Sens. Mag.*, vol. 3, no. 2, pp. 8–23, Jun. 2015.
- [19] V. Mrstik, “Effects of phase and amplitude quantization errors on hybrid phased-array reflector antennas,” *IEEE Trans. Antennas Propag.*, vol. 30, no. 6, pp. 1233–1236, Nov. 1982.
- [20] J. R. Piepmeier *et al.*, “SMAP L-band microwave radiometer: Instrument design and first year on orbit,” *IEEE Trans. Geosci. Remote Sens.*, vol. 55, no. 4, pp. 1954–1966, Apr. 2017.
- [21] S. Riendeau and C. Grenier, “RADARSAT-2 antenna,” in *Proc. IEEE Aerosp. Conf.*, Mar. 2007, pp. 1–9.
- [22] L. Rondinelli, “Effects of random errors on the performance of antenna arrays of many elements,” in *Proc. IRE Int. Conv. Rec.*, vol. 7, Mar. 1958, pp. 174–189.
- [23] A. Rosenqvist, M. Shimada, N. Ito, and M. Watanabe, “ALOS PALSAR: A pathfinder mission for global-scale monitoring of the environment,” *IEEE Trans. Geosci. Remote Sens.*, vol. 45, no. 11, pp. 3307–3316, Nov. 2007.
- [24] F. Rostan, S. Riegger, W. Pitz, R. Croci, and R. Torres, “The C-SAR instrument design & performance for the GMES Sentinel-1 mission,” in *Proc. 7th Eur. Conf. Synth. Aperture Radar (EUSAR)*, Jun. 2008, pp. 1–4.

- [25] V. Shahmirian and A. S. Daryoush, "Pattern degradation due to random errors in active phased array antennas," in *Dig. Antennas Propag. Soc. Int. Symp.*, vol. 1, Jun. 1989, pp. 396–399.
- [26] F. T. Ulaby and M. Dobson, *Handbook of Radar Scattering Statistics for Terrain*. Norwood, MA, USA: Artech House, 1989.
- [27] M. Villano, G. Krieger, and A. Moreira, "New insights into ambiguities in quad-pol SAR," *IEEE Trans. Geosci. Remote Sens.*, vol. 55, no. 6, pp. 3287–3308, Jun. 2017.
- [28] H. S. C. Wang, "A comparison of the performance of reflector and phased-array antennas under error conditions," in *IEEE Aerosp. Appl. Conf. Dig.*, Feb. 1991, p. 4-1.



Sigurd Huber received the Dipl.Ing. (M.S.) degree in electrical and communication engineering from the Technical University of Munich (TUM), Munich, Germany, in 2005, and the Dr.Ing. (Ph.D.) degree (Hons.) in electrical and communication engineering from the Karlsruhe Institute of Technology (KIT), Karlsruhe, Germany, in 2014.

Since 2005, he has been with the Microwaves and Radar Institute, German Aerospace Center (DLR), Oberpfaffenhofen, Germany, where he is engaged in the conception of future SAR systems, utilizing advanced multichannel antenna architectures. He is involved in national and international projects in the field of Earth observation, encompassing cooperations with industry partners (Airbus, Germany, and OHB, Germany) and research organizations (ESA, NASA/JPL, and JAXA). For the German Earth observation mission proposal Tandem-L, he has been responsible for the SAR system and performance engineering. From 2018 to 2019, he has served as the Project Manager in the Phase-A and Phase-B1 studies for the mission proposal ROSE-L in the frame of ESA's Copernicus Programme. He is the author or a coauthor of more than 70 publications in international conferences and journals. He holds a patent on array-fed reflector antennas for synthetic aperture radar applications. His research interests, in general, include classical and quantum field theory and more specifically digital signal processing, inverse problems, array processing, antenna theory, and quantum optics.



Marwan Younis (Fellow, IEEE) received the B.Sc. degree in electrical engineering from the University of Baghdad, Baghdad, Iraq, in 1992, and the Dipl.Ing. (M.Sc.) and Dr.Ing. (Ph.D.) degrees in electrical engineering from the Universität Karlsruhe (TH), Karlsruhe, Germany, in 1997 and 2004, respectively.

In 1996, he was an Intern with the Jet Propulsion Laboratory (JPL), Pasadena, CA, USA, where he spent research sabbaticals in 2013 and 2019. From 1998 to 2004, he was a Research Scientist with the Institut für Höchstfrequenztechnik und Elektronik, Universität Karlsruhe. Since 2005, he has been with the Microwaves and Radar Institute, German Aerospace Center (DLR), Oberpfaffenhofen, Germany. He is also the Head of the SAR Techniques Group, DLR, and a Professor of spaceborne radar systems with the Karlsruhe Institute for Technology (KIT), Karlsruhe. He is the author or a coauthor of about 180 conference papers and 40 reviewed publications. He holds five patents. His research fields include synthetic aperture radar (SAR) systems and techniques, MIMO SAR, digital beamforming, SAR performance, calibration, and antennas.

Dr. Younis is also an active member of the IEEE and currently serving the GRSS AdCom. He received the Hermann-Billing Award for his Ph.D. thesis in 2005. He also co-chairs the Instrumentation and Future Technologies GRSS Technical Committee. He is also a reviewer of IEEE publications. He was an Associate Editor for the IEEE GEOSCIENCE AND REMOTE SENSING LETTERS from 2012 to 2019.



Gerhard Krieger (Fellow, IEEE) received the Dipl.Ing. (M.S.) and Dr.Ing. (Ph.D.) (Hons.) degrees in electrical and communication engineering from the Technical University of Munich, Munich, Germany, in 1992 and 1999, respectively.

From 1992 to 1999, he was with the Ludwig Maximilian University, Munich, where he conducted multidisciplinary research on neuronal modeling and nonlinear information processing in biological and technical vision systems. Since 1999, he has been with the Microwaves and Radar Institute, German

Aerospace Center (DLR), Oberpfaffenhofen, Germany, where he started as a Research Associate developing signal processing algorithms for a novel forward-looking radar system employing digital beamforming on receive. From 2001 to 2007, he led the New SAR Missions Group, Microwaves and Radar Institute, German Aerospace Center, that pioneered the development of advanced bistatic and multistatic radar systems, such as TanDEM-X, as well as innovative multichannel SAR techniques and algorithms for high-resolution wide-swath SAR imaging. Since 2008, he has been the Head of the Radar Concepts Department, Microwaves and Radar Institute, German Aerospace Center, that hosts about 40 scientists focusing on new SAR techniques, missions, and applications. He has been serving as a Mission Engineer for TanDEM-X. He also made major contributions to the development of the Tandem-L Mission Concept, where he led the Phase-0 and Phase-A studies. Since 2019, he has been a Professor with the Friedrich-Alexander-University Erlangen, Erlangen, Germany. He is also the author or a coauthor of more than 90 peer-reviewed journal papers, 9 invited book chapters, and about 400 conference papers. He more than 15 patents.

Prof. Krieger received several national and international awards, including the W. R. G. Baker Prize Paper Award from the IEEE Board of Directors, two Transactions Prize Paper Awards of the IEEE Geoscience and Remote Sensing Society, and two Best Paper Awards at the European Conference on Synthetic Aperture Radar. In 2014, he has served as the Technical Program Chair of the European Conference on Synthetic Aperture Radar and as a Guest Editor for the IEEE JOURNAL OF SELECTED TOPICS IN APPLIED EARTH OBSERVATIONS AND REMOTE SENSING. He has been an Associate Editor of the IEEE TRANSACTIONS ON GEOSCIENCE AND REMOTE SENSING since 2012.



Alberto Moreira (Fellow, IEEE) received the B.S.E.E. and M.S.E.E. degrees from the Aeronautical Technological Institute (ITA), São José dos Campos, Brazil, in 1984 and 1986, respectively, and the Dr.Eng. degree (Hons.) from the Technical University of Munich, Munich, Germany, in 1993.

From 1996 to 2001, he was the Chief Scientist and Engineer with the SAR Technology Department, German Aerospace Center (DLR), Oberpfaffenhofen, Germany. Under his leadership, the DLR airborne SAR system has been upgraded to operate in innovative imaging modes, such as polarimetric SAR interferometry, tomography, and holography. Since 2001, he has been the Director of the Microwaves and Radar Institute, DLR, and a Full Professor of microwave remote sensing with the Karlsruhe Institute of Technology (KIT), Karlsruhe, Germany. His DLR's Institute contributes to several scientific programs and projects for spaceborne SAR missions, such as TerraSAR-X, TanDEM-X, SAR-Lupe, and SARah, as well as Kompsat-6, PAZ, Sentinel-1, BIOMASS, and ROSE-L. The mission TanDEM-X, led by his institute, has generated a global, high-resolution digital elevation model of the Earth with unprecedented accuracy. He is the initiator and a principal investigator (PI) for this mission. He is the author or a coauthor of more than 450 publications in international conferences and journals and eight book chapters. He holds more than 40 international patent grants in the radar and antenna field. His professional interests and research areas encompass spaceborne radar end-to-end system design, microwave techniques and system concepts, signal processing, and remote sensing applications.

Dr. Moreira was a recipient of several international awards, including the IEEE AESS Nathanson Award in 1999 for the Young Radar Engineer of the Year, the IEEE Kiyo Tomiyasu Field Award in 2007, the IEEE W. R. G. Baker Award from the IEEE Board of Directors in 2012, and the IEEE GRSS Distinguished Achievement Award in 2014. He and his colleagues received the GRSS Transactions Prize Paper Awards in 1997, 2001, and 2007 and the GRSS Letters Prize Paper Award in 2015 and 2017. He has served as the President of the IEEE Geoscience and Remote Sensing (GRS) Society in 2010 and the General Co-Chair of IGARSS in 2012. He has been serving as the Chair of the Major Awards of the GRS Society since 2017. He was the Founder and the Chair of the GRSS German Chapter from 2003 to 2008 and has served as an Associate Editor for the IEEE GRS LETTERS from 2003 to 2007 and the IEEE TRANSACTIONS ON GEOSCIENCE AND REMOTE SENSING since 2005. From 2012 to 2017, he has served as a Principal Investigator for the Helmholtz Alliance Remote Sensing and Earth System Dynamics and is currently the PI for Tandem-L, a radar mission proposal for the global observation of dynamic processes on Earth's surface with unprecedented quality and resolution.